Systematic research on the formation of heterogenous microstructure in FeCoNiCrMn high entropy cold spray

Pengfei Yu, Ningsong Fan, Shuo Yin, Rocco Lupoi

Trinity College Dublin, The University of Dublin, Department of Mechanical, Manufacturing and Biomedical Engineering, Parsons Building, Dublin 2, Ireland

Abstract

High entropy alloys, as a novel alloy system, demonstrated excellent mechanical performance. However, despite its excellent mechanical performance, the strength-ductility trade-off effect still limit its performance. In recent decades, it has been found that heterogenous or gradient microstructure can efficiently solve the conflict. Cold spray is a promising method to create heterogenous microstructure with high efficiency and low cost. In this work, equiatomic FeCoNiCrMn HEA was deposited by cold spray and the microstructure was systematically investigated by transmission electron microscopy (TEM) and transmission Kikuchi diffraction (TKD). In cold spray, a gradient microstructure was formed and segregated Ni and Mn in starting particle were also redistributed. Moreover, twinning in ultra-fine nanograins were detected in the region close to the impact interface. Compared with severe deformation of other low SFE metals, for FeCoNiCrMn HEA, twinning in nanograins also highly related to the grain size.

Introduction

In recent years, high entropy alloys (HEA) by taking the concept of multiple principal elements (typically five or more) have been designed and they exhibit a combination of excellent mechanical properties, superior wear resistance and corrosion resistance, which makes HEA as a promising engineer material (Ref 1,2). Among the various HEA alloys, the equiatomic single FCC phase FeCoNiCrMn, also known as Cantor alloy, has been widely studied (Ref 3–5). In comparison to the conventional metal, Cantor alloy has less trade-off effect between high strength and ductility and consequently has excellent toughness even under extreme low temperature condition (Ref 6–10). The outstanding mechanical properties of Cantor alloy are attributed to its multiple strengthening mechanism (Ref 1). The equiatomic composition cause large distortion in lattice, which results in outstanding solution strengthening (Ref 1). Furthermore, it has also been found that during the deformation of Cantor alloy, it demonstrates multiple deformation pathways (Ref 10–14). In addition to dislocation gliding, phase transition and twinning induce plasticity also occur. Latest research found that crystalline to amorphous transition happened once the Cantor alloy was deformed with strain rate over 10^6 s^{-1}(Ref 13).

Because of the excellent performance of FeCoNiCrMn HEA, different techniques have been taken to fabricate FeCoNiCrMn coating to explore the application of FeCoNiCrMn on surface protection (Ref 15). Among these techniques, cold spray (CS), a kind of solid-state deposit technique that achieve the deposit via micron particles bonding through the severe deformation induced by supersonic impact, minimizes the influence of oxidization and has an excellent deposit efficiency(Ref 16,17). Moreover, recently, CS has been regarded as a promising additive manufacture technology(Ref 18). In cold spray, the micron size powder particles will be mixed with heated high-pressure gas and then flow through a de-Laval nozzle. After that, the particle is accelerated to the speed of supersonic and impact on the substrate or previous deposited particles. During the supersonic impact, an extreme deformation condition with strain rate over 10^8 s^{-1} will occur, which results in severe strain hardening and grain refinement (Ref 16,19,20). As introduced above, the microstructure evolution of FeCoNiCrMn in the deformation has obvious strain rate sensitivity. Therefore, the influence of extreme deformation in CS on the microstructure of FeCoNiCrMn after CS process should be investigated, which is highly related to the bonding mechanism and CS deposit performance.

However, up to now, there are still lack of studies on this regime. Yin et al. (Ref 21) firstly fabricated FeCoNiCrMn coatings by using CS methods and the coating exhibited great improvement in hardness. They attributed the increase of hardness to severe strain hardening and grain refinement during the extreme

deformation in CS process. Nikbakht et al. (Ref 22)conduct detail investigation on the microstructure of FeCoNiCrMn particle after the impact in CS by using Electron channelling contrast im-aging (ECCI) and electron backscatter diffraction (EBSD). In addition to the dislocation density increase and grain refinement, they also found the evidence of nanotwinning and they further inferred that amorphization may occur during the impact, which may provide extra strain hardening mechanism for CS HEA deposit. But limited by the capability of ECCI and EBSD, the microstructure information in the region close to the impact interface where deformation is the severest is impossible to obtain due to the extreme grain refinement and high crystalline defects. It is also not plausible to conclude occurrence of amorphization due to the occurrence of nanotwinning. Therefore, more detail investigation should be conducted to get clearer acknowledge on the microstructure evolution in region close to the impact interface in CS process, which not only help us understand the bonding mechanism in CS of FeCoNiCrMn HEA, but also can explore the changes on microstructure once FeCoNiCrMn is deformed with an extreme deformation condition.

Methodology

The cold spray process of FeCoNiCrMn HEA particles was conducted by using an in-house supersonic spray system available in Trinity College Dublin. Compressed helium was used as the propulsive gas. The inlet gas pressure and temperature were 3.0 MPa and 300 ℃, respectively. The de-Laval nozzle has a round cross-sectional shape with a divergent length of 180 mm. The throat and outlet diameters are 2 mm and 6 mm, respectively. By using this system, the HEA particles were sped up/accelerated to the supersonic velocity and directly impacted onto an Al substrate. The velocity and temperature of the HEA particles upon impact were estimated ranging from 797 to 1253 m/s, and 180℃ to 338 ℃ based on a robust CFD model developed for cold spray simulation.

The CrMnFeCoNi powders used in this work were supplied by Vilory Advanced Materials Technology Ltd, China. The powders had spherical shape and size range from 15 and 53 μm. Fig. 1 shows the morphology of a CrMnFeCoNi powder and electron backscatter diffraction (EBSD) inverse pole figure (IPF) map showing the cross-sectional grain structure of a powder. The average grain size of the particles was approximately 1.37μm. Fig. 1b shows the high-angle annular dark-field (HADDF) image and the corresponding energy dispersive spectroscopy (EDS) mapping of a starting FeCoNiCrMn particle. As can be seen, the five principal elements were homogeneously distributed in most regions, while Mn and Ni were segregated in the boundaries of cell structures.

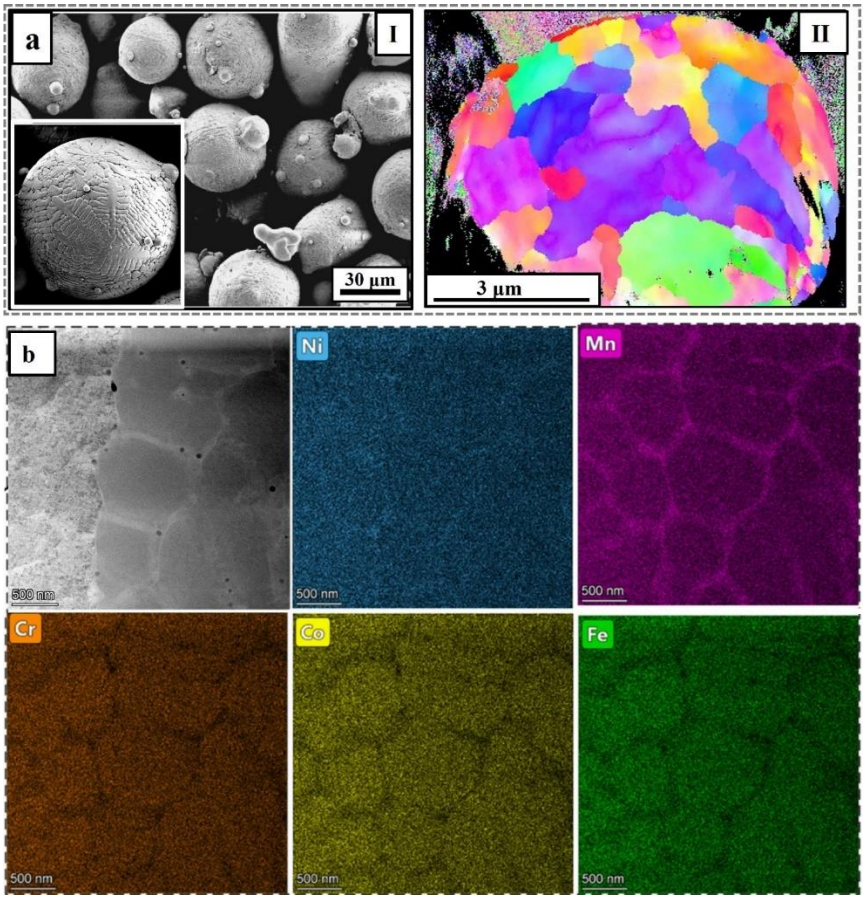

Fig.1. Characterization of the FeCoNiCrMn powder used in this work. (a) surface morphology and EBSD IPF map showing the cross-sectional grain structure of a particle, and (b) HADDF and EDS mapping of a starting powder cross-section showing segregated elements in the boundaries of cell structures

In order to investigate the microstructure evolution of the CrMnFeCoNi HEA after ultra-high strain rate deformation, a TEM foil specimen was prepared by focused ion beam (FIB) from the interfacial region between adjacent particles where HEA experienced the highest strain rate during deformation. The FIB operation was performed on Carl Zeiss ULTRA Plus scanning electron microscopy (SEM) equipped with the FIB device (FEI Scios). The FIB-prepared foil specimen was then studied on FEI Tecnai G2 F20 transmission electron microscopy (TEM) equipped with the EDS detector (Oxford Instruments). The EDS mapping was conducted on the foil specimen at the interfacial region to reveal the element evolution during ultra-high strain rate deformation. In addition, the foil specimen was also characterized by transmission Kikuchi diffraction (TKD) through SEM equipped with EBSD detector (Oxford Instruments) and TKD holder to obtain inverse pole figure (IPF) map, band contrast image and Kernel average misorientation map (KAM).

Finite element analysis (FEA) was used to estimate the strain, strain rate and temperature at the highly deformed interparticle interfacial region since the current technologies are unable to experimentally measure the strain rate and temperature in such an extreme condition, i.e. supersonic impact of micro-sized particles. The model used in this work was a mature single-particle-impact model which has been widely used and validated. The model was constructed into 3D representation, and Johnson-cook constitutive model was used to describe the particle and substrate material properties. The minimum (15 µm) and maximum (53 µm) particle sizes were selected and simulated to cover the entire particle size range. The corresponding impact velocity and temperature were taken from the CFD calculations. The simulated deformation parameters were extracted from the same position as the FIB-prepared foil for TEM characterization.

Results and discussion

Formation of ultra-fine grain structure

Fig.2 shows the BF-TEM and TKD images of a highly deformed region in the vicinity of an interparticle interface to demonstrate the different grain structures resulting from the extreme deformation during the supersonic impact of the particle. The interparticle interface is highlighted with red arrows in Fig. 2a. The TKD images shown in Fig. 2b are taken from the region marked by the dash-line square in Fig. 2a. As compared to the homogenous grain structure in starting powders (Fig. 1), a gradient grain structure and significant grain refinement occurred in the selected region. It is seen that the grain structure depended on the relative location to the interface. Along the impact direction from the interface to the particle interior, three characteristic zones can be identified based on the grain structures morphology and grain size, namely, ultrafine-grain zone (UG), lamellar grain zone (LG), and highly deformed grain zone (HDG). The formation of such diverse grain structures was the consequence of thermal-mechanical variations in these regions. Before the discussion, the average grain size, simulated strain rate and temperature in the three characteristic zones were listed in the Table.1. Moreover, because in the deformation work hardening and thermal softening effect induced by high strain rate and rising of temperature respectively can compete with each other and decide the stress condition, to have better understand on the thermal-mechanical condition in three zones, Zener-Holloman parameter that described the comprehensive effect of strain rate and temperature was calculated and it is expressed as (Ref 23):

$$Z = \dot{\varepsilon}\exp(Q / RT)$$

Here, $\dot{\varepsilon}$ is strain rate, T is deformation temperature and Q is deformation energy of the materials. A higher Z value indicates that the strain rate is high, or temperature is low and work hardening predominates. The natural logarithms of Z in three characteristic zones were given in the Table.1

Table 1. Summary of the average grain size, strain, simulated strain rate, temperature and lnZ in the three characteristic zones

Position	Average grain size, nm	Strain	Strain gradient	Simulated strain rate, s-1	Simulated temperature, K	lnZ
Staring particle	1370	0	0	0	293	~
HDG	619	0.96~1.16	0.16	$1.13\sim0.8\times10^8$	1000~1145	70
LSG	156	1.12~1.42	0.33	$1.85\sim1.96\times10^8$	1043~1187	64
UG	60.3	1.45~1.86	0.44	$3.40\sim4.18\times10^8$	1108~1243	73

In the HDG zone, the strain rate and temperature were the lowest among the three zones, but the plastic deformation was still large enough to evolve the coarse grains of the starting powders into small grains with the size of hundreds of nanometres as revealed by the TKD images (Fig. 2b). The TEM image in Fig. 2c reveals severely tangled dislocations in small grains and nanotwins in large grains as marked by red arrows, which suggests high dislocation density and low grain boundary mobility in this zone. The high strain rate in this region was one of reasons that led to a high dislocation density (Ref 24). Despite the high strain rate, it should also be noted that the strain gradient in HDG was about 0.16 μm-1 and because the density of GNDs increases with strain gradient, such high strain gradient can induce a larger amount of geometrically necessary dislocations (GNDs) (Ref 25). Moreover, it has been found that the GNDs density decreases with grain size increasing and GNDs density is consequently higher in smaller grains (Ref 25,26). In addition, for the CrMnFeCoNi HEA, its low stacking fault energy suppressed the occurrence of cross slip of dislocations, and thus the dislocations could not be dissipated via dynamic recovery. The sluggish effect of the HEA hindered the movement of dislocations. Moreover, lnZ in HDG is higher than that in LG but the strain rate in HDG is lower. Thus, the higher lnZ was the result of lower thermal softening effect due to the lower temperature in HDG. This thermal-mechanical condition in HDG weakened the mobility of dislocation and grain boundary, which consequently suppressed further dissipation of dislocations via dynamic

recrystallization in the deformation. All these factors worked together to cause the dislocations continuously accumulated and severely tangled in small grains.

In the LG zone, the temperature and strain rate were higher than those in the HDG zone. Owing to a higher strain rate, more dislocations were produced and resulted in a higher dislocation density. Moreover, with strain increasing, the strain gradient in LG was higher than HDG and thus, more GNDs formed. Consequently, the dislocation density in LG was higher than that in HDG zone. However, it can be seen that the lnZ is the lowest in three zones, which indicated the predominance of thermal softening effect, and the mobility of dislocation and grain boundary were improved. With deformation going on, due to the higher grain boundary migration, as shown in the TKD images (Fig.2b), grains in the LG zone were deformed into lamellar shape parallel to the interface and some lamellar grains were even deformed into the thickness of tens of nanometres. With grains getting smaller, GNDs density became higher. Because of the improvement of dislocation mobility, high-density dislocations got more chances to interact with each other and form cell structures that can be seen clearly from the TEM image shown in Fig. 2d and are marked by green arrows. Some of cell structures in thinner grain were separated for lamellar grains when these grains were deformed into the thickness that was equal to the size of dislocation cells, which made lamellar grains subdivided into several sections as marked by white circle in Fig.2b. The separated cells further rotated with increasing strain and finally form nanograins with large angle grain boundaries, for example the grain marked by white circle in Fig.2d.

In the UG zone, the strain, strain rate and temperature simultaneously reached their maximum value, Therefore, the grain structure in UG was dramatically different from that in other two zones. As shown in Fig.2e, equiaxed grains with average size of 60 nm fully covered the UG zone. Most of the nanograins were free of dislocations, which indicated that these grains were produced by a complete DRX process (Ref 27). Although deformation temperature was extremely high in the UG zone, lnZ instantly increased to higher value which indicates strain hardening effect overwhelmed thermal softening effect. With the assistance of highest strain rate and strain gradient, the dislocations density in the UG can be the highest in three zones at the early stage of the deformation and smallest cell structures were consequently formed previous to the DRX process. The ultra-fine cell structures then rotated with the deformation process or directly bulged out of grain boundaries, finally resulting in the formation of ultra-fine DRX nanograin (Ref 28,29).

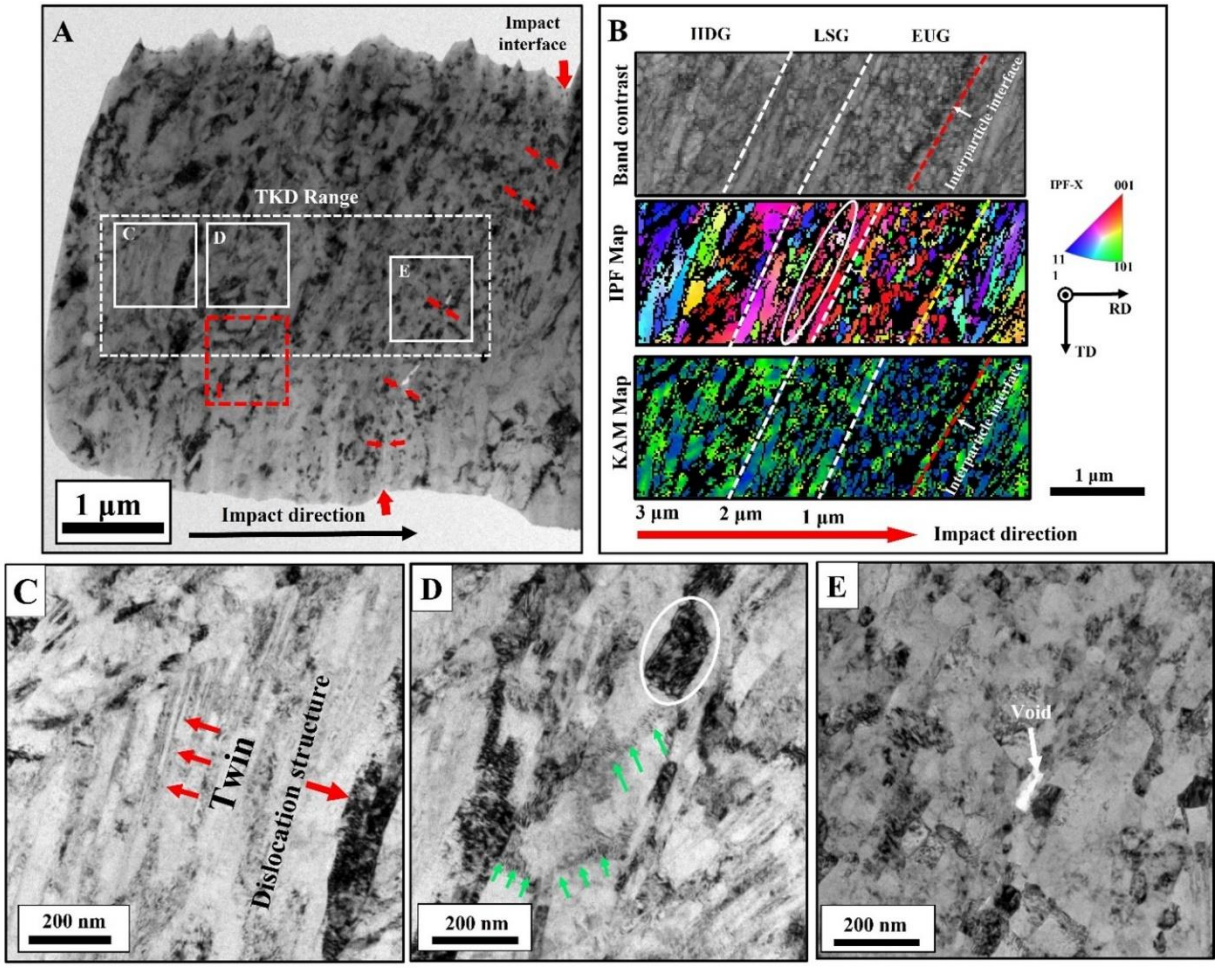

Fig. 2. Characterization of the highly deformed region of FeCoNiCrMn after extreme deformation. (a) BF-TEM image showing the overall microstructure, the characteristic regions and magnified microstructures (Fig. 2ai and Fig. 2aii) (b) TKD map showing the three characteristic regions. The TKD image was taken from the selected zone marked as white square in the BF-TEM image (Fig. 2a). The interparticle interface was marked by red and yellow dash lines in the IPF map and KAM maps respectively

Formation of twins

In addition to the grain structure refinement, as shown in BF-TEM images in Fig.2c and Fig.2d, which were respectively taken from the HDG zones and boundary between the HDG and LSG zones, nanotwins (marked by red arrows) were also formed in the refined grain structure. Previous research found that in the normal deformation (room temperature and low strain rate), the twinning cannot be detected if the average grain size is smaller than 500 nm (Ref 30). By applying a more severe plastic deformation condition like split Hopkinson pressure bar, nanotwins can be found in the grains with size of ~100 nm, but its density was quite low (Ref 6). Herein, the average grain size in the HDG and the LSG orderly decreased from 619 nm to 156 nm, but the twinning was still detectable/apparent and had a high density, which indicated that an ultra-high strain rate deformation in CS process expanded the regime of deformation twinning to smaller grains regime despite the reduction of flow stress caused by thermal softening effect. With distance getting close to the impact interface, the deformation became severer, and the average grain size was gradually refined towards less than 100 nm. As shown in Fig 2e, due to a more complete DRX process, there were no clear dislocation structures that could be found in HDG and LG. Furthermore, although in this region the strain and strain rate were higher than that in the HDG and LG zones, twinning was not detectable anymore. Although, for FeCoNiCrMn HEA, twinning has been robustly proved as an essential deformation mechanism due to its low stacking fault energy, the occurrence of deformation twinning becomes tougher

with grain size decreasing, which is also known as the grain effect on twinning (Ref 31,32). Herein, the gradual disappearance of twinning indicated that this grain size effect on twinning also happened in the deformation of FeCoNiCrMn HEA. And it is plausible to infer that it is the grain size effect that prohibit the occurrence of twinning in LG zone. However, as shown in Fig.3, it is interesting to find that when the position came to the impact interface where the strain rate and temperature were both maximum, grains were further refined to smaller than 50 nm, and nanotwins appeared again (marked by red arrows). The maximum strain rate in this region was sufficiently high to overcome the hindrance of grain size effect and induce the occurrence of twinning.

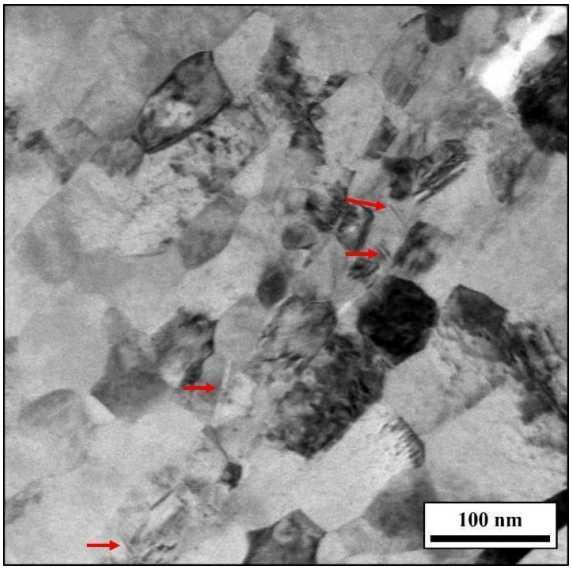

Fig. 3. BF-TEM image showing some twins in nanograins in the EUG zone. Nanograins were highlighted with red arrows.

In spite of the occurrence of twinning in ultra-fine nanograins, on the contrary to previous experiments and molecular dynamic modelling investigation, in which amorphization and FCC to HCP phase transition have been found after ultra-high strain rate deformation, in this work, both in TKD and TEM characterization results, there was no direct evidence to prove the occurrence of amorphization and FCC to HCP phase transition. It is noted that the majority of previous research were conducted at room temperature or low temperature. Therefore, the influence of temperature was minimized. Here, because of the rapid temperature increasing caused by the heat generation in the severe plastic deformation, atoms were thermally activated. Therefore, more crystalline defects were activated and the migration of crystalline interface became easier, which resulted in the occurrence of DRX. During the DRX process, a lot of deformation energy was dissipated. Moreover, nanograins formed after DRX process in ultra-high strain rate deformation could induce grain boundary mediated deformation, which further consume a part of deformation energy. As the consequence of that, the remained deformation energy was not enough to trigger the amorphous and phase transition.

Segregated elements redistribution

Fig. 4a and 4b demonstrate the BF-TEM images and the corresponding EDS maps taken from the region I (in the boundary between HDG and LG region) and region E (in the UG region) marked by red dash-lines in Fig. 2a. By comparing the undeformed starting powder with the highly deformed region, one can notice that the Mn-Ni segregation evolved from network style (Fig. 1b) into ribbon-like concentrated style (Fig. 4a and 4b). These Mn-Ni-enriched ribbons mainly concentrated in the laminar grains as indicated by the red dash lines in the BF-TEM images, and they were separated by thicker grains. In addition, the thickness of Mn-Ni-enriched ribbons is thinner than that in the starting particle. However, it is interesting to note that the Mn-Ni-enriched ribbons could not be found in the equiaxed nanograins of the UG region as marked by two green lines in Fig. 4b. This phenomenon indicated the outstanding redistribution of segregated elements and the occurrence of long-distance atomic diffusion. But it should be noted that the deformation process here was finished within 30~60 ns that was too short for atoms to achieve a long-distance diffusion only by

bulk diffusion. Moreover, one can also find that nanoscale Mn-rich precipitation with other element depleted appears in the triple joint of laminar grains as marked by the white circles in Fig. 4a, which is also detected in the UG zone but has smaller size. Precipitation and decomposition phenomenon after long-time annealing of deformed FeCoNiCrMn has been widely reported and investigated (Ref 14,33,34). Therefore, the mechanism of segregated Mn-Ni redistribution and the formation of Mn-rich precipitation observed in this study must be different from previous reports, and these will be discussed in the following text.

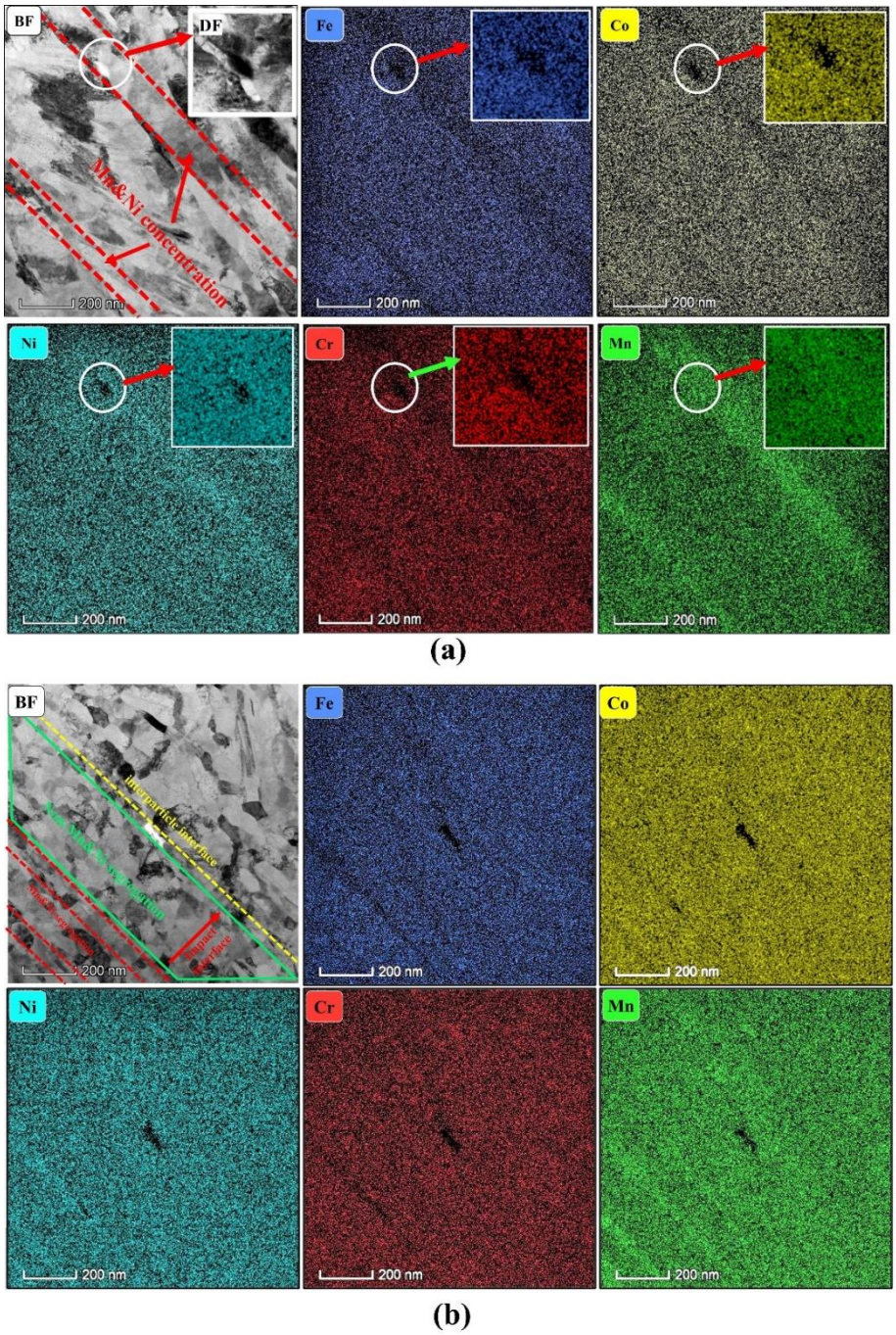

Fig. 4. EDS maps showing the element distribution of the regions selected from Fig. 2a. (a) EDS map for region I, and (b) EDS map for region II. Dark-filed (DF) TEM showing the Mn precipitate at the triple joint of laminar grains was provided in the top-right corner of the BF-TEM image in Fig. 3a. The grain structures

having segregated Ni and Mn were marked by red lines in the BF-TEM images. Mn precipitates were marked by white circle.

In the rapid solidification process, dendrite as shown in Fig.1a was easy to form. Mn and Ni concentrated in the interdendrite due to their low melting temperature(Ref 3,35–38). Moreover, the segregation of low melting Mn and Ni elements induced large shrinkage stress and caused the twisting or rotation of dendrite, which consequently resulted in the formation of low angle grain boundaries (LAGB) in the interdendrite where Mn and Ni were concentrated (Ref 39,40). Therefore, the Mn-Ni segregated cell structure as shown in Fig.1b is the cross-section of dendrite in Fig.1a and can be treated as subgrains due to its low angle grain boundaries.

Fig.5 shows the schematic to explain the element redistribution process during the extreme deformation. At the beginning, Mn and Ni were segregated in the interdendrite and subgrain boundaries were formed in the starting powders (Fig. 5a). During the impact-induced extreme deformation, subgrains with Mn-Ni concentrated LAGB evolved into high angle grain boundaries (HAGB) via continuous rotation, and the average grain size decreased. Due to the grain refinement in the deformation, grain boundary area considerably increased. It has been found that Mn had the highest diffusion rate among the five principal elements in FeCoNiCrMn and the sluggish diffusion of Ni vanished when Ni atoms diffused along the grain boundary (Ref 41–43). Therefore, long distance atomic migration was prone to occur for Mn and Ni in FeCoNiCrMn. The large area of grain boundaries provided a large number of shortcuts for the diffusion of Ni and Mn. Thus, the segregated Ni and Mn diffused along newly formed grain boundaries (Fig. 5b-f). Since this process was accompanied by grain structure evolution in the extreme deformation, segregated elements can wildly disperse in the newly formed grain boundary network within tens of nanoseconds. At the same time, the segregated Mn and Ni in the grain boundaries also created an elemental concentration gradient decreasing from the grain boundary to the inner part of the grain, which provided a driving force for the segregated elements to diffuse from grain boundaries into the grain interior (Fig. 5e-f). Meanwhile, the deformation-induced high temperature intensified the atomic vibration and production of vacancies, which cut down the energy barrier for atomic diffusion. These factors worked together to promote the Ni and Mn diffusing from the grain boundaries into the grains.

For the equiaxed nanograins in the UG region, the grains were heavily refined to less than 100 nm and grain boundary area was much higher than in the other regions. The temperature was the highest among three regions as well. Thus, the segregated Ni and Mn can instantly diffuse along the grain boundaries and quickly diffuse into the grain interior as shown in Fig.5e, which finally results in a homogenous compositional distribution. In the other regions, the grain size was larger, and consequently the concentration gradient of the segregated elements was lower, which led to a lower diffusion driving force. Meanwhile, the temperature in these regions was lower as addressed in Table 1, which weakened the atomic migration. Therefore, the inward diffusion from the grain boundary to the grain interior was suppressed.

However, as compared to the equiaxed nanograin region in the UG region, the other regions had higher dislocation density. It is interesting to noted that the lamellar grain circled on the right side of the BF images in Fig.4a has higher dislocation density than that in the neighbour grain structure on the left side and the thick Mn ribbon was located in the grains with higher dislocation density (larger TEM image can be found in Supplementary Document), which indicated the redistribution is related to the dislocation density. It is known that dislocations can act as tunnels for atomic diffusion since they could reduce the energy barrier for diffusion by dissipating their stored strain energy (Ref 44). In this case, the role of dislocation density in diffusion became apparent in the LG, HDG and the rest of the UG regions. Furthermore, it is known that, for a single grain in polycrystalline material, dislocation density near the grain boundary is higher than that in the grain interior (Ref 45). Herein, high strain rate induces a high dislocation multiplication rate and the ultra-high strain gradient resulted in the formation of GNDS, which consequently promoted the dislocation accumulation. The highly accumulated dislocations in the grain boundary provided extra pathways for segregated Mn and Ni atoms to diffuse into the inner part of the grain, which partially compensated for the negative effect of lower temperature and the reduction of diffusion driving force due to increased grain size. For a thinner grain, it had higher dislocation density than larger grain due to their small volume and higher GNDs density. Moreover, compared with coarser grains, the concentration gradient of Mn and Ni in thinner grains was also higher, which led to higher diffusion driving force. Consequently, as described in Fig. 5e, segregated elements were prone to diffuse into thinner grains. Finally, the microstructure that has two

thinner ribbon-like Mn and Ni enriched grains separated by a thicker grain having less outstanding element enrichment was formed (Fig. 4).

As for the Mn-rich precipitation observed in the triple joint of grains (Fig. 4a), it can be seen in Fig. 1b that the concentration of segregated elements in the cell boundaries was inhomogeneous. Atomic diffusion rate in grain boundaries could be influenced by grain boundaries area and misorientations (Ref 46). Therefore, during the grain structure evolution, the concentration of segregated elements could not redistribute homogeneously in the grain boundary network. In certain positions, the concentration of segregated elements may be sufficiently high to trigger precipitation nucleation. Because this process occurred in grain boundaries, the formation of precipitation was promoted due to heterogeneous nucleation. In the triple joint of grains, heterogeneous nucleation was more prone to occur (Ref 33,47). Consequently, Mn-rich precipitation was mainly detected in the triple joint of grains as shown in Fig. 4a.

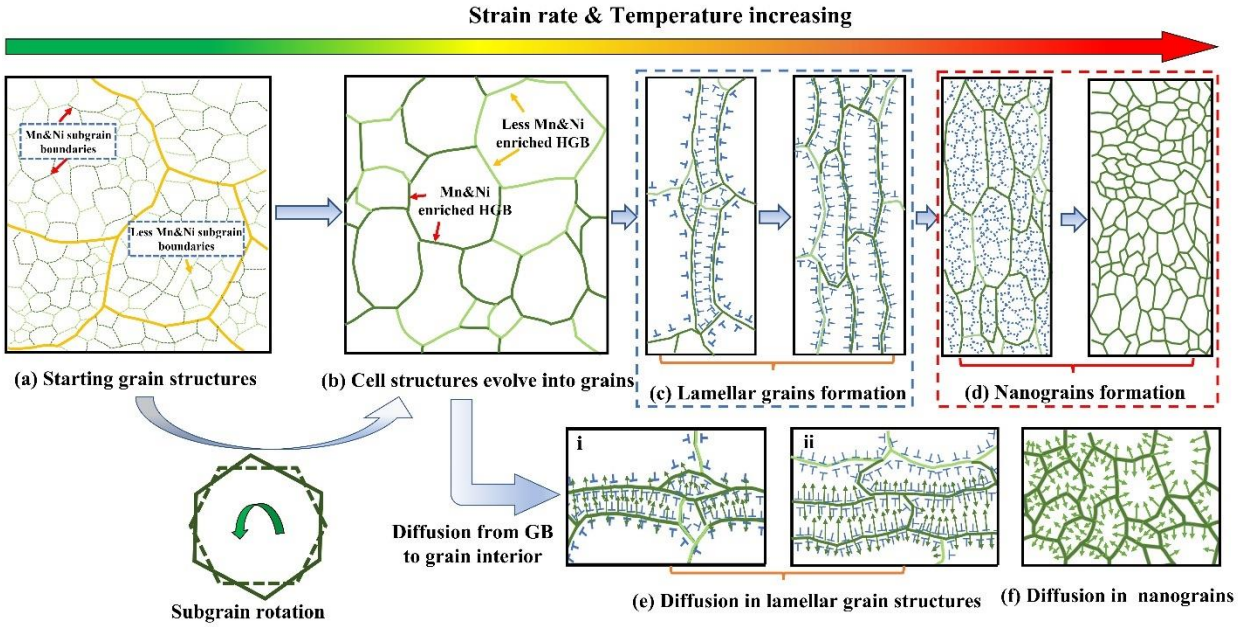

Fig. 4. Schematic showing the redistribution process of the Mn and Ni elements during extreme deformation. (a) Mn and Ni are initially segregated in interdendrite and subgrains are formed; (b) with deformation going on, low angle grain boundary subgrains become high angle grain boundaries; (c) newly formed grains are deformed into laminar shape; (d) When the deformation becomes severest, large amounts of substructures are formed and transferred into equiaxed nanograins. At the same time segregated Ni and Mn diffusion along the grain boundary and create concentration gradient between the grain boundary and interior; (e) in the laminar grains, atoms diffuse into thinner grain; (f) in equiaxed DRX grain, segregated elements uniformly diffuse into nanograins.

Conclusion

In this work, FeCoNiCrMn HEA was deposited by cold spray techniques. High resolution characterization technology TKD and TEM was taken to investigate the microstructure evolution in the region close to the impact interface.

1. Due to ultra-high strain rate and extreme large strain gradient, a gradient grain structure with average grain size range from 60nm to over 600nm was formed. Ultra-fine grain with size smaller than 50nm was also formed in the vicinity of impact interface was detected.
2. Nanotwinning occurred in the cold spray process and the occurrence of twinning demonstrated obvious grain size effect. The propensity of twinning gradually decreased from the inner part of particle to the impact interface with grain size decreasing and twinning disappear when the grain

size was smaller than 100nm. However, due to maximum strain rate in impact interface, the deformation here was extreme enough to trigger the twinning process and resulted the occurrence of twinning.

3. Because of higher deformation temperature, DRX was easy to happen, which dissipated a majority of deformation energy. Thus, the rest of energy was too low to induce further FCC to HCP phase transition and amorphization.
4. The segregated Mn and Ni in starting particle could rapidly redistribute with the microstructure evolution during deformation in the impact process. The high density of dislocation induced by high strain rate and severe increase of grain boundary resulted from DRX provided extra pathways for the diffusion of segregated Mn and Ni.

Reference

1. E.P. George, D. Raabe, and R.O. Ritchie, High-Entropy Alloys, *Nature Reviews Materials*, 2019, **4**(8), p 515–534.

2. Y. Zhang, T.T. Zuo, Z. Tang, M.C. Gao, K.A. Dahmen, P.K. Liaw, and Z.P. Lu, Microstructures and Properties of High-Entropy Alloys, *Progress in materials science*, Elsevier, 2014, **61**, p 1–93.

3. B. Cantor, I.T.H. Chang, P. Knight, and A.J.B. Vincent, Microstructural Development in Equiatomic Multicomponent Alloys, *Materials Science and Engineering: A*, 2004, **375–377**, p 213–218.

4. N.L. Okamoto, S. Fujimoto, Y. Kambara, M. Kawamura, Z.M.T. Chen, H. Matsunoshita, K. Tanaka, H. Inui, and E.P. George, Size Effect, Critical Resolved Shear Stress, Stacking Fault Energy, and Solid Solution Strengthening in the CrMnFeCoNi High-Entropy Alloy, *Scientific Reports*, 2016, **6**(1), p 35863.

5. Y. Zhang, T.T. Zuo, Z. Tang, M.C. Gao, K.A. Dahmen, P.K. Liaw, and Z.P. Lu, Microstructures and Properties of High-Entropy Alloys, *Progress in materials science*, Elsevier, 2014, **61**, p 1–93.

6. Z. Li, S. Zhao, S.M. Alotaibi, Y. Liu, B. Wang, and M.A. Meyers, Adiabatic Shear Localization in the CrMnFeCoNi High-Entropy Alloy, *Acta Materialia*, Elsevier, 2018, **151**, p 424–431.

7. E.P. George, W.A. Curtin, and C.C. Tasan, High Entropy Alloys: A Focused Review of Mechanical Properties and Deformation Mechanisms, *Acta Materialia*, 2020, **188**, p 435–474.

8. B. Gludovatz, A. Hohenwarter, D. Catoor, E.H. Chang, E.P. George, and R.O. Ritchie, A Fracture-Resistant High-Entropy Alloy for Cryogenic Applications, *Science*, American Association for the Advancement of Science, 2014, **345**(6201), p 1153–1158.

9. Z.R. Zhang, D.E.J. Armstrong, and P.S. Grant, The Effects of Irradiation on CrMnFeCoNi High-Entropy Alloy and Its Derivatives, *PROGRESS IN MATERIALS SCIENCE*, 2022, **123**.

10. F. Otto, A. Dlouhý, Ch. Somsen, H. Bei, G. Eggeler, and E.P. George, The Influences of Temperature and Microstructure on the Tensile Properties of a CoCrFeMnNi High-Entropy Alloy, *Acta Materialia*, 2013, **61**(15), p 5743–5755.

11. S. Zhao, Z. Li, C. Zhu, W. Yang, Z. Zhang, D.E.J. Armstrong, P.S. Grant, R.O. Ritchie, and M.A. Meyers, Amorphization in Extreme Deformation of the CrMnFeCoNi High-Entropy Alloy, *Science advances*, American Association for the Advancement of Science, 2021, **7**(5), p eabb3108.

12. U. Lee, B. Straumal, and N. Park, Dynamic Precipitation of σ-Phase and Element Partitioning in Equiatomic CoCrFeMnNi High-Entropy Alloy, *Materials Science and Engineering: A*, Elsevier, 2021, **804**, p 140739.

13. H. Wang, D. Chen, X. An, Y. Zhang, S. Sun, Y. Tian, Z. Zhang, A. Wang, J. Liu, and M. Song, Deformation-Induced Crystalline-to-Amorphous Phase Transformation in a CrMnFeCoNi High-

Entropy Alloy, *Science Advances*, American Association for the Advancement of Science, 2021, **7**(14), p eabe3105.

14. J.M. Park, J. Moon, J.W. Bae, M.J. Jang, J. Park, S. Lee, and H.S. Kim, Strain Rate Effects of Dynamic Compressive Deformation on Mechanical Properties and Microstructure of CoCrFeMnNi High-Entropy Alloy, *Materials Science and Engineering: A*, Elsevier, 2018, **719**, p 155–163.

15. A. Meghwal, A. Anupam, B.S. Murty, C.C. Berndt, R.S. Kottada, and A.S.M. Ang, Thermal Spray High-Entropy Alloy Coatings: A Review, *Journal of Thermal Spray Technology*, 2020, **29**(5), p 857–893.

16. H. Assadi, H. Kreye, F. Gärtner, and T. Klassen, Cold Spraying–A Materials Perspective, *Acta Materialia*, Elsevier, 2016, **116**, p 382–407.

17. H. Assadi, F. Gärtner, T. Stoltenhoff, and H. Kreye, Bonding Mechanism in Cold Gas Spraying, *Acta Materialia*, 2003, **51**(15), p 4379–4394.

18. W. Li, K. Yang, S. Yin, X. Yang, Y. Xu, and R. Lupoi, Solid-State Additive Manufacturing and Repairing by Cold Spraying: A Review, *Journal of materials science & technology*, Elsevier, 2018, **34**(3), p 440–457.

19. P.C. King, S.H. Zahiri, and M. Jahedi, Microstructural Refinement within a Cold-Sprayed Copper Particle, *Metallurgical and Materials Transactions A*, 2009, **40**(9), p 2115–2123.

20. S. Yin, X.F. Wang, X.K. Suo, H.L. Liao, Z.W. Guo, W.Y. Li, and C. Coddet, Deposition Behavior of Thermally Softened Copper Particles in Cold Spraying, *Acta Materialia*, 2013, **61**(14), p 5105–5118.

21. S. Yin, W. Li, B. Song, X. Yan, M. Kuang, Y. Xu, K. Wen, and R. Lupoi, Deposition of FeCoNiCrMn High Entropy Alloy (HEA) Coating via Cold Spraying, *Journal of Materials Science & Technology*, Elsevier, 2019, **35**(6), p 1003–1007.

22. R. Nikbakht, M. Saadati, T.-S. Kim, M. Jahazi, H.S. Kim, and B. Jodoin, Cold Spray Deposition Characteristic and Bonding of CrMnCoFeNi High Entropy Alloy, *Surface and Coatings Technology*, 2021, **425**, p 127748.

23. F.J. Humphreys and M. Hatherly, “Recrystallization and Related Annealing Phenomena,” Elsevier, 2012.

24. E.I.G.-N. and J.S. and P.E.J. Rivera-Díaz-del-Castillo, Dislocation Annihilation in Plastic Deformation: II. Kocks–Mecking Analysis, *Acta Materialia*, 2012, **60**(6–7), p 2615–2624.

25. N.A. Fleck, G.M. Muller, M.F. Ashby, and J.W. Hutchinson, Strain Gradient Plasticity: Theory and Experiment, *Acta Metallurgica et materialia*, Elsevier, 1994, **42**(2), p 475–487.

26. Z.H. Jiang, J.S. Lian, And B. Baudelet, A Dislocation Density Approximation For The Flow Stress-Grain Size Relation Of Polycrystals, *Acta Metallurgica Et Materialia*, 1995, **43**(9), p 3349–3360.

27. K. Huang and R.E. Logé, A Review of Dynamic Recrystallization Phenomena in Metallic Materials, *Materials & Design*, 2016, **111**(dec.5), p 548–574.

28. M.E. Kassner and S.R. Barrabes, New Developments in Geometric Dynamic Recrystallization, *Materials ence & Engineering A*, 2005, **410**(Nov), p 152–155.

29. Z.Y. Liu, H.Z. Wang, M. Hache, E. Irissou, and Y. Zou, Formation of Refined Grains below 10 Nm in Size and Nanoscale Interlocking in the Particle-Particle Interfacial Regions of Cold Sprayed Pure Aluminum, *Scripta Materialia*, 2020, **177**, p 96–100.

30. S.J. Sun, Y.Z. Tian, H.R. Lin, H.J. Yang, X.G. Dong, Y.H. Wang, and Z.F. Zhang, Transition of Twinning Behavior in CoCrFeMnNi High Entropy Alloy with Grain Refinement, *Materials Science and Engineering: A*, Elsevier, 2018, **712**, p 603–607.

31. X.L. Wu and Y.T. Zhu, Inverse Grain-Size Effect on Twinning in Nanocrystalline Ni, *Physical review letters*, APS, 2008, **101**(2), p 25503.

32. Y.T. Zhu, X.Z. Liao, and X.L. Wu, Deformation Twinning in Nanocrystalline Materials, *Progress In Materials Science*, 2012, **57**(1), p 1–62.

33. F. Otto, A. Dlouhý, K.G. Pradeep, M. Kuběnová, D. Raabe, G. Eggeler, and E.P. George, Decomposition of the Single-Phase High-Entropy Alloy CrMnFeCoNi after Prolonged Anneals at Intermediate Temperatures, *Acta Materialia*, 2016, **112**, p 40–52.

34. B. Schuh, F. Mendez-Martin, B. Völker, E.P. George, H. Clemens, R. Pippan, and A. Hohenwarter, Mechanical Properties, Microstructure and Thermal Stability of a Nanocrystalline CoCrFeMnNi High-Entropy Alloy after Severe Plastic Deformation, *Acta Materialia*, 2015, **96**, p 258–268.

35. M. Laurent-Brocq, A. Akhatova, L. Perrière, S. Chebini, X. Sauvage, E. Leroy, and Y. Champion, Insights into the Phase Diagram of the CrMnFeCoNi High Entropy Alloy, *Acta Materialia*, 2015, **88**, p 355–365.

36. K.G. Prashanth and J. Eckert, Formation of Metastable Cellular Microstructures in Selective Laser Melted Alloys, *Journal of Alloys and Compounds*, 2017, **707**, p 27–34.

37. Y.M. Wang, T. Voisin, J.T. McKeown, J. Ye, N.P. Calta, Z. Li, Z. Zeng, Y. Zhang, W. Chen, T.T. Roehling, R.T. Ott, M.K. Santala, P.J. Depond, M.J. Matthews, A. V Hamza, and T. Zhu, Additively Manufactured Hierarchical Stainless Steels with High Strength and Ductility, *Nature Materials*, 2018, **17**(1), p 63–71.

38. Z.G. Zhu, Q.B. Nguyen, F.L. Ng, X.H. An, X.Z. Liao, P.K. Liaw, S.M.L. Nai, and J. Wei, Hierarchical Microstructure and Strengthening Mechanisms of a CoCrFeNiMn High Entropy Alloy Additively Manufactured by Selective Laser Melting, *Scripta Materialia*, Elsevier, 2018, **154**, p 20–24.

39. R.E. Napolitano and R.J. Schaefer, The Convergence-Fault Mechanism for Low-Angle Boundary Formation in Single-Crystal Castings, *Journal of materials science*, Springer, 2000, **35**(7), p 1641–1659.

40. A. Wagner, B.A. Shollock, and M. McLean, Grain Structure Development in Directional Solidification of Nickel-Base Superalloys, *Materials Science and Engineering: A*, Elsevier, 2004, **374**(1–2), p 270–279.

41. Y. Zhang, T. Bian, X. Shen, Z. Wang, S. Ye, S. Feng, K. Yu, C. Ding, and P. Yu, Sintering Mechanism and Microstructure Evolution of a CoCrFeNiMn High Entropy Alloy Fabricated by Metal Injection Molding, *Journal of Alloys and Compounds*, Elsevier, 2021, **868**, p 158711.

42. X.C. Liu, H.W. Zhang, and K. Lu, Strain-Induced Ultrahard and Ultrastable Nanolaminated Structure in Nickel, *Science*, American Association for the Advancement of Science, 2013, **342**(6156), p 337–340.

43. D.L. Beke and G. Erdélyi, On the Diffusion in High-Entropy Alloys, *Materials Letters*, 2016, **164**, p 111–113.

44. E.W. Hart, On the Role of Dislocations in Bulk Diffusion, *Acta Metallurgica*, 1957, **5**(10), p 597.

45. F.J. Humphreys and M. Hatherly, Chapter 4 - The Structure and Energy of Grain Boundaries, F.J. Humphreys and M.B.T.-R. and R.A.P. (Second E. Hatherly, Eds., (Oxford), Elsevier, 2004, p 91–119.

46. A. Paul, T. Laurila, V. Vuorinen, and S. V Divinski, “Thermodynamics, Diffusion and the Kirkendall Effect in Solids,” Springer, 2014.

47. M. Glienke, M. Vaidya, K. Gururaj, L. Daum, B. Tas, L. Rogal, K.G. Pradeep, S. V Divinski, and G. Wilde, Grain Boundary Diffusion in CoCrFeMnNi High Entropy Alloy: Kinetic Hints towards a Phase Decomposition, *Acta Materialia*, 2020, **195**, p 304–316.